Journal of Physics and Chemistry of Solids 93 (2016) 1–6

Contents lists available at ScienceDirect

Journal of Physics and Chemistry of Solids

journal homepage: www.elsevier.com/locate/jpcs

Hard magnetic properties of nanosized $Sr(Fe,Al)_{12}O_{19}$ hexaferrites obtained by Pechini method

V. Barrera, I. Betancourt *

Departamento de Materiales Metálicos y Cerámicos, Instituto de Investigaciones en Materiales, Universidad Nacional Autónoma de México, México D.F. 04510, México

ARTICLE INFO

Article history:
Received 2 October 2015
Received in revised form
26 January 2016
Accepted 8 February 2016
Available online 9 February 2016

Keywords:
A. Magnetic materials
A. Ceramics
B. Chemical synthesis
C. X-ray diffraction
D. Magnetic properties

ABSTRACT

In this work, we report the magnetic properties of isotropic M-type $SrFe_{12-x}Al_xO_{19}$ ($x=0.0,1.5$) hexaferrites synthesized by means of Pechini method. A polycrystalline distribution of fine grains was verified by Transmission Electron Microscopy for both compositions, with average sizes below 60 nm. Remarkable coercivity values within the range 500–850 kA/m were attained as a consequence of a combined effect of grain size refinement together with an enhancement of the anisotropy field afforded by the incorporation of the Al^{3+} cations into the hexagonal crystal structure.

1. Introduction

Permanent magnets are an important class of functional materials due to their wide technological application field, including small motors, actuators, generators, medical and microwave devices, and more recently, emerging applications related to automobile industry [1,2]. Hard ferrites with magnetoplumbite structure (also known as M-type hexaferrites) occupies a significant place in the permanent magnet market due to their competitive cost per unit of stored energy, their excellent chemical stability and their high Curie temperature, usually well above 600 K [3–6]. These materials have been widely used for fabrication of decoration magnets or as anisotropic components in loudspeakers or small motors. In addition, the considerable magnetocrystalline anisotropy characteristic of the hexagonal M-type structure favors typically coercivity field values of around 400 kA/m, which falls within the low field range of nanocomposite Nd–Fe–B hard magnets with low rare earth content (i.e., below 8 at%) [7,8]. Although numerous partial Sr/Fe substitutions have been extensively reported for $SrFe_{12}O_{19}$ ferrites with variable effect on their magnetic performance [5,9,10], the best choice for attaining coercivity values in excess of 400 kA/m is partial Fe replacement by Al, for which coercivity values as high as 800 kA/m have been reported [10,11]. Coercivity indicates the ability of the material to resist demagnetization reversal under the application of an external field. Other figures of merit to evaluate the magnetic performance of permanent magnets are the remanence magnetization and the saturation magnetization [1,2,7].

An important number of synthetic routes have been reported for obtaining pure and doped M-type hexaferrites with variable coercivity values, like self-combustion method, solid state reaction, sol–gel, co-precipitation and polymerizable complex method, among others [3–5,9,12]. An alternative way to obtain nanosized hexaferrites is the “Pechini method”. In this synthetic route, an alpha hydroxycarboxylic acid (like citric acid) is used to chelate with various cationic precursors by forming a polybasic acid. In the presence of a polyhydroxyl alcohol like (ethylene glycol), the chelate reacts to form organic esters and water by-products. When the mixture is heated, polyesterification occurs and leads to a homogeneous sol in which metal ions are uniformly distributed throughout the organic matrix. When the sol is further heated to remove the excess of solvents, an intermediate resin will be formed. The solid resin is then heated to elevated temperatures to remove organic residuals. The aimed stoichiometric compounds are formed during the pyrolysis. Due to the homogeneity of the ions spreading, as well as the formation of small particles with narrow size distribution, the diffusion of cations towards the formation of the product phase is feasible for reaction temperatures lower than 1000 °C [13]. In this work, we report and discuss the magnetic properties of nanosized $Sr(Fe,Al)_{12}O_{19}$ hexaferrites obtained by means of the Pechini method by using calcination

* Corresponding author.
E-mail address: israelb@unam.mx (I. Betancourt).

http://dx.doi.org/10.1016/j.jpcs.2016.02.007
0022-3697/

temperatures below 1000 °C, alongside coercivity enhancement over 800 kA/m.

2. Experimental techniques

M-type hexaferrites with formula $SrFe_{12-x}Al_xO_{19}$ (x=0.0, 1.5) were synthesized by means of the Pechini method. The following precursors were used: $Fe(NO_3)_3 \cdot 9H_2O$ (Mallinckrodt, ≥99.0%), $Sr(NO)_2$ (Fluka ≥99.0%) and $Al(NO)_2 \cdot 6H_2O$ (Aldrich ≥98.0%). The synthetic route was the following: For each nitrate, weighed according to the stoichiometry of each composition, an individual dissolution in distilled water was prepared. After two hours of stirring, all the dissolutions were mixed in a single one. The polymeric resin was formed separately by the addition of citric acid and ethyleneglycol in the molar proportion 1:14, by heating at 70 °C during 30 min. At this point, the nitrates dissolution was added to the resin and kept under continuous stirring during 3 h at 90 °C, until the water evaporated. The resultant dried polymer was grounded for the following sequence of calcination treatments in a muffla (Thermolyne 47900): 200 °C for 12 h, 400 °C for 4 h, 700 °C for 18 h and 800 °C for 24 h. These synthetic conditions are milder than those reported for equivalent $SrFe_{12-x}Al_xO_{19}$ hexaferrites in [10,11], for which annealing temperatures ≥950 °C were used, alongside hydrochloric acid for dissolving the glassy matrix in one case. The proposed reaction for the $SrFe_{12}O_{19}$ hexaferrite is the following:

$$2{\cdot}Sr(NO_3)_2 + 24{\cdot}(1-x)Fe(NO_3)_3{\cdot}9H_2O \rightarrow 2{\cdot}SrFe_{12}O_{19} + 38{\cdot}N_2 + 216{\cdot}H_2O + 95{\cdot}O_2$$

Phase distribution and grain size features were determined by means of XRD diffraction in a Bruker AXS D8 equipment with Co-K_α radiation and by using Transmission Electron Microscopy (TEM) in a JEOL 1200 equipment operating at 20 kV. Additionally, grain morphology was verified by Scanning Electron Microcopy in a Jeol F7600 equipment. The magnetic properties at room temperature were determined by means of Vibrating Sample Magnetometry (VSM) in a LDJ 9600 equipment with H_{max}=1250 kA/m, whereas the Curie temperature was established by means of Magnetic Thermogravimetric Analysis (MTGA) in a thermobalance within the temperature range 300–980 K at a heating rate of 10 K/min under an applied field of 160 kA/m.

3. Results

X-ray diffractograms for the $SrFe_{12-x}Al_xO_{19}$ hexaferrites are shown in Fig. 1. All the peaks correspond to the hexagonal M-type $SrFe_{12}O_{19}$ phase, according to the ICDD file # 01-084-1531. No extra peaks related to secondary phases are observed. The Al^{3+} substitution into the hexagonal crystal structure is expected to occur due to the accomplishment of the rule of charge conservation [6].

Rietveld analysis was performed for both compositions in order to verify the formation of a single phase, as shown in Fig. 2 for the $SrFe_{10.5}Al_{1.5}O_{19}$ hexaferrite as example. The contribution of the sample holder (made of SiO_2) was taken into account for the fitting process at low angles, giving an excellent match with experimental data, as indicated by all the R factors (R_{exp}, R_{wp}, R_p and χ^2) shown in Table 1, together with the structural parameters resulting from the fitting process (for both compositions). Additionally, the refined atomic positions and the occupation factors for all the crystallographic sites as well as the bond distance together with the bond angle, are displayed for the $SrFe_{12}O_{19}$ hexaferrite in Tables 2 and 3. For the $SrFe_{10.5}Al_{1.5}O_{19}$ sample, same data are displayed in Tables 4 and 5.

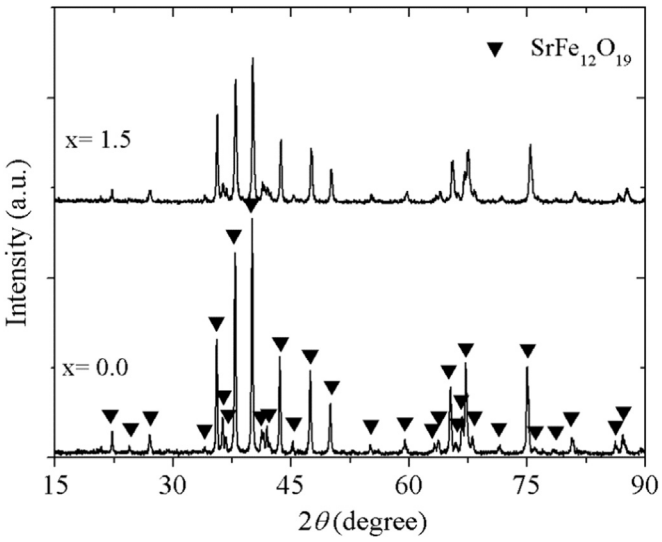

Fig. 1. X-ray diffractograms for the $SrFe_{12-x}Al_xO_{19}$ hexaferrites.

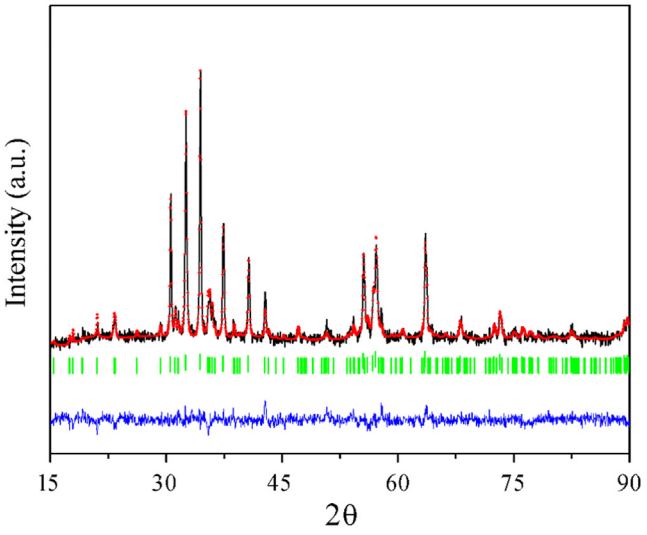

Fig. 2. Experimental (solid black line) and calculated (dots in red) X-ray diffraction profiles for the $SrFe_{10.5}Al_{1.5}O_{19}$ hexaferrite. Tick marks below the diffraction pattern represent the allowed Bragg reflections. The difference profile is located at the bottom of the figure as a blue line. (For interpretation of the references to color in this figure legend, the reader is referred to the web version of this article.)

Table 1
Structural parameters and R factors from Rietveld analysis for $SrFe_{12-x}Al_xO_{19}$ hexaferrites.

Parameter	$SrFe_{12}O_{19}$	$SrFe_{10.5}Al_{1.5}O_{19}$
Unit cell (Å)	a=5.891, c=23.084	a=5.855, c=22.969
Crystallite size (nm)	61.4	58.9
Volume (Å^3)	693.7	682.1
Density (g/cm^3)	5.08	4.95
R_{exp} (%)	1.703	1.775
R_{wp} (%)	3.604	2.270
R_p (%)	2.6	1.812
χ^2	2.117	1.279

$SrFe_{12}O_{19}$ hexaferrite has a magnetoplumbite-type crystal structure, comprising alternative stacks of spinel S (Fe_6O_8) and hexagonal R ($SrFe_6O_{11}$) blocks in the form of RSR^*S^*, where * denotes 180° rotation around the hexagonal c-axis. Within the unit

Table 2
Refined atomic positions and occupation factors for all the crystallographic sites for the $SrFe_{12}O_{19}$ hexaferrite.

Átom	Site	x	y	z	SOF
Sr	4e	0.6666	0.3333	0.2500	1
Fe1	2a	0.0000	0.0000	0.0000	1
Fe2	2b	0.0000	0.0000	0.2736	1
Fe3	4f1	0.3333	0.6666	0.0395	1
Fe4	4f2	0.3333	0.6666	0.1951	1
Fe5	12k	0.1689	0.3358	0.1118	1
O1	4e	0.0000	0.0000	0.2636	1
O2	4f	0.3333	0.6666	−0.0639	1
O3	6h	0.1817	0.3285	0.2500	1
O4	12k	0.1565	0.2703	0.0674	1
O5	12k	0.5047	0.9989	0.1688	1

Table 3
Bond distance and bond angle for the $SrFe_{12}O_{19}$ hexaferrite.

Type	Bond distance (Å)	Type	Bond distance (Å)	Type	Bond angle (deg.)
Sr–O3	2.843	Fe4–O5	1.801	Fe2–O1–Fe5	147.1
Sr–O5	2.534	Fe5–O2	2.019	Fe2–O3–Fe5	88.6
Fe1–O4	2.083	Fe5–O4	1.983	Fe3–O2–Fe5	123.3
Fe2–O3	1.766	Fe5–O5	2.122	Fe1–O4–Fe5	89.90
Fe3–O2	2.389	Fe2–Fe5	3.150	Fe5–O4–Fe5	97.44
Fe3–O4	1.879	Fe4–Fe4	2.531		
Fe4–O3	2.142	Fe5–Fe5	2.930		

Table 4
Refined atomic positions and occupation factors for all the crystallographic sites for the $SrFe_{10.5}Al_{1.5}O_{19}$ hexaferrite.

Átom	Site	x	y	z	SOF
Sr	4e	0.6666	0.3333	0.2500	1
Fe1	2a	0.0000	0.0000	0.0000	1
Fe2	2b	0.0000	0.0000	0.2628	0.49
Al2	2b	0.0000	0.0000	0.2628	0.51
Fe3	4f1	0.3333	0.6666	0.0266	1
Fe4	4f2	0.3333	0.6666	0.1898	1
Fe5	12k	0.1746	0.3522	0.8919	0.0024
Al5	12k	0.1746	0.3522	0.8919	0.9976
O1	4e	0.0000	0.0000	0.1516	1
O2	4f	0.6666	0.3333	0.0705	1
O3	6h	0.1619	0.3521	0.2500	1
O4	12k	0.1987	0.2796	0.0486	1
O5	12k	0.5666	0.0089	0.1449	1

cell, 24 Fe^{3+} ions occupy five different crystallographic sites of oxygen lattice: one tetrahedral ($4f_1$), three octahedral ($12k$, $2a$, $4f_2$) and one hexahedral ($2b$) sites. The spins of Fe^{3+} ions in these sites are ferromagnetically coupled through superexchange interaction with the oxygen ions, causing the spins in $2a$, $12k$, and $2b$ sites to align parallel to the crystallographic c axis and those in $4f_1$ and $4f_2$ sites to align anti-parallel. For the Rietveld refinement of $SrFe_{10.5}Al_{1.5}O_{19}$, Al^{3+} replaced Fe^{3+} cations at the sites 2b and 12k. According to our calculated site occupation factors (SOF), Al^{3+} ions preferably substitute Fe^{3+} at the 12k site, whereas at the 2b site, half of the Fe^{3+} ions are replaced by Al^{3+}. Since the Al^{3+} electronic configuration is [Ne] $2s^2$ $2p^6$, the full p-band implies non-magnetic contribution and thus, a noticeable decrease of the magnetic moment is expected after Fe^{3+} replacement by Al^{3+} cations. This reduction was confirmed by our magnetic measurements, as shown in the following sections. The unit cell decreased after Al-substitution, as indicated by the reduction of its volume (from 693.73 $Å^3$ for $x=0.0$, to 682.1 $Å^3$ for $x=1$. See Table 1). The observed reduction for the crystal structure can be ascribed to the difference between Fe^{3+} and Al^{3+} ionic radius $\langle r\rangle$ in octahedral coordination ($\langle r_{Fe3+}\rangle$= 0.645 Å and $\langle r_{Al3+}\rangle$=0.535 Å [14]). This alteration of the unit cell also affects the geometry of the trigonal bipyramid interstitial site occupied by M^{3+} ions (Fe and Al) at the 2b site with fivefold coordination (of oxygen atoms), for which an increased O3–M^{3+} bond distance is observed, alongside an enlarged O1–M^{3+}–O3 angle, as shown in Table 6.

Complementary, TEM observations indicated the formation of a polycrystalline, randomly-oriented distribution of polyhedral grains, as illustrated in Figs. 3 and 4 for $SrFe_{12-x}Al_xO_{19}$ hexaferrites. The corresponding Selected Area Electron Diffraction (SAED) pattern is included as inset for both samples. The formation of Debye–Scherrer rings reflects the random orientation of the nanosized crystals. All the indexed diffracting planes correspond to the hexagonal crystal structure of the $SrFe_{12}O_{19}$ phase, which is consistent with XRD results. An average grain size of 60 ± 45 nm and 58.3 ± 10.0 nm was estimated for samples with $x=0$ and $x=1.5$, respectively. The significant uncertainty reflects the rather broad grain size distribution resulting from the synthetic route used.

Additionally, SEM micrographs for the $SrFe_{12}O_{19}$ hexaferrite is shown in Fig. 5. This image was generated by using secondary electrons, thus affording a better visualization of the grain morphology. More defined grains with polyhedral characteristics were confirmed, together with a noticeable grain size variation, including several grains of 100 nm, which is congruent with the broad grain size distribution determined from TEM observations. For the $SrFe_{10.5}Al_{1.5}O_{19}$ composition, a very similar grain morphology was observed (not shown).

Hysteresis M–H loops for both $SrFe_{12-x}Al_xO_{19}$ ($x=0.0,1.5$) hexaferrites are shown in Fig. 6. No magnetic saturation is observed in

Table 5
Bond distance and bond angle for the $SrFe_{10.5}Al_{1.5}O_{19}$ hexaferrite.

Type	Bond distance (Å)	Type	Bond distance (Å)	Type	Bond angle (deg.)
Sr–O3	2.854	Fe5–O4	2.400	Fe1–O4–Fe5	87.60
Sr–O5	2.943	Fe5–O5	2.110	Fe1–O4–Al5	87.60
Fe1–O4	1.838	Fe1–Fe5	3.057	Fe4–O5–Fe4	120.17
Fe2–O1	2.556	Fe4–Fe4	2.763	Fe5–O1–Fe5	140.09
Fe2–O3	1.812	Fe5–Fe5	2.762	Fe5–O4–Fe5	91.40
Fe3–O2	2.233	Al2–O1	2.556	O1–Al2–O3	99.38
Fe3–O4	2.056	Al2–O3	1.812	O1–Fe5–O4	89.50
Fe4–O3	2.112	Al5–O1	2.048	O2–Fe5–O4	91.30
Fe4–O5	2.051	Al5–O2	1.812	O2–Fe5–O5	89.8
Fe5–O1	2.048	Al5–O4	2.400	O1–Al5–O4	89.50
Fe5–O2	1.812	Al5–O5	2.110	O2–Al5–O4	91.30
				O2–Al5–O5	89.8

Table 6
Bond distance and bond angle comparison at the trigonal bipyramid interstitial site for $SrFe_{12-x}Al_xO_{19}$ hexaferrites. This site is denoted as 2b and the corresponding Fe^{3+}/Al^{3+} ions are labeled as Fe2 and Al2, as in Tables 2–5.

Composition	O3–M^{3+} (Å)	O1–M^{3+}–O3 (deg.)
$SrFe_{12}O_{19}$	1.766 M=Fe2	72.00 M=Fe2
$SrAl_{1.5}Fe_{10.5}O_{19}$	1.812 M=Al2	99.38 M=Al2

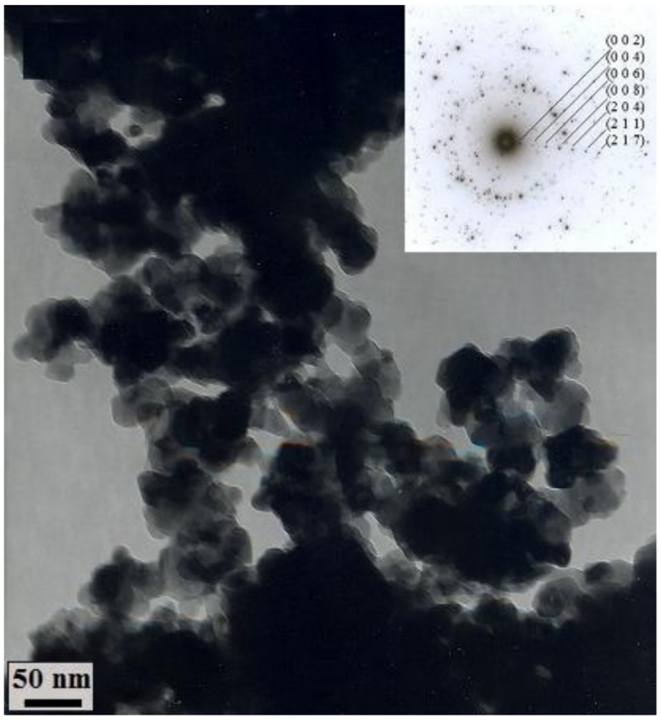

Fig. 3. TEM micrograph for the $SrFe_{12}O_{19}$ hexaferrite. Inset: Selected Area Electron Diffraction pattern.

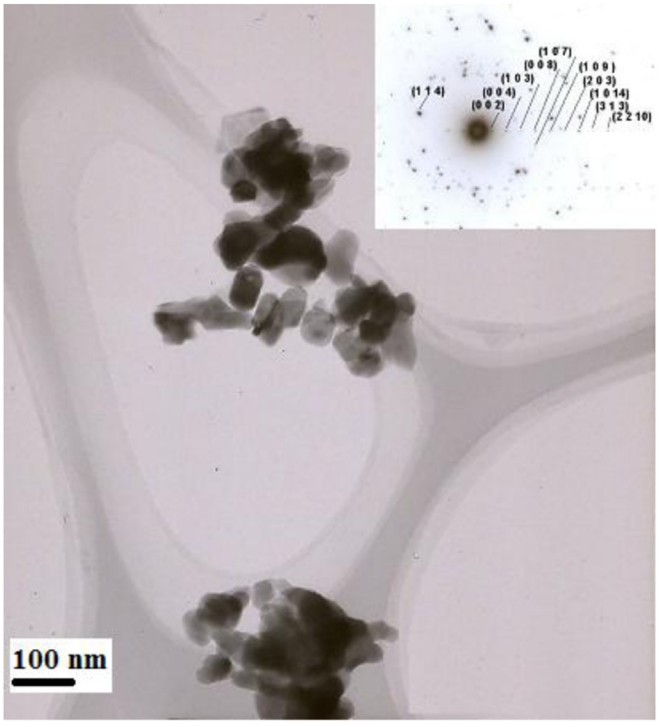

Fig. 4. TEM micrograph for the $SrFe_{10.5}Al_{1.5}O_{19}$ hexaferrite. Inset: Selected Area Electron Diffraction pattern.

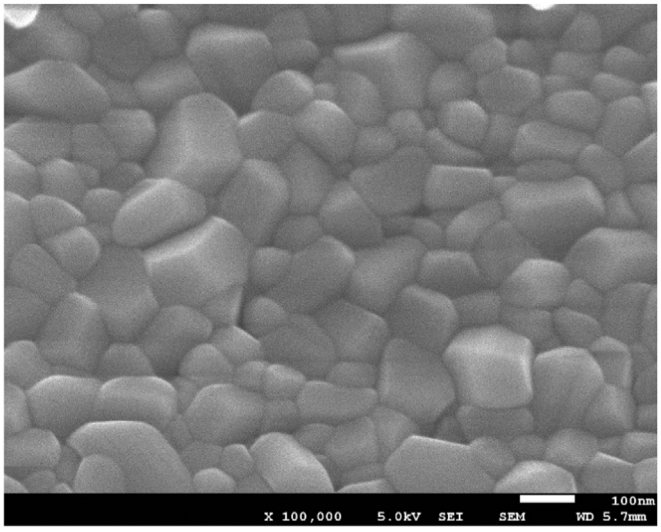

Fig. 5. SEM micrograph for the $SrFe_{12}O_{19}$ hexaferrite (imaged formed with secondary electrons).

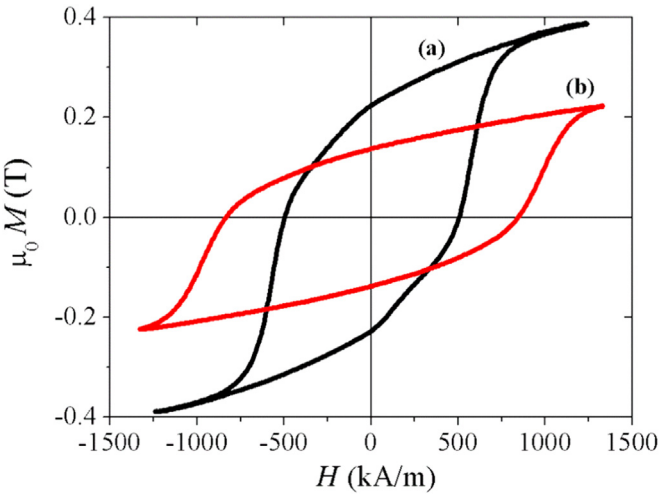

Fig. 6. Hysteresis $M-H$ loops for $SrFe_{12-x}Al_xO_{19}$ hexaferrites: (a) $x=0.0$ (b) $x=1.5$.

any case at the maximum field H available in our equipment. Marked reductions for the maximum magnetization $\mu_0 M_{max}$, as well as for the remanence magnetization $\mu_0 M_r$, were observed for the Al-containing sample compared with the initial $SrFe_{12}O_{19}$. For the $SrFe_{12}O_{19}$ sample, a subtle step is visible on the demagnetizing section of the M–H curve, which can be attributed to the noticeable grain size variation within this sample. According to TEM observations, the rather wide uncertainty determined for the average grain size (60 ± 45 nm) implies that big particles (of 100 nm) are interspersed among small ones (lower than 50 nm). This fact was confirmed by SEM micrograph of Fig. 5. Large grains hinder the interparticle exchange coupling, since they possess a lower fraction (relative to small grains) of surface magnetic moments to be exchange coupled with magnetic moments of adjacent grains. As a result, a decoupling effect is visible as a subtle step on the demagnetizing section of the hysteresis loop. On the other hand, the $SrFe_{10.5}Al_{1.5}O_{19}$ sample exhibits a well defined demagnetizing quadrant with monotonous behavior, which reflects some degree of intergrain exchange coupling interaction acting between grains, promoted by the narrower grain size distribution indicated by the error interval of the main size value estimated from TEM observations (of 58.3 ± 10.0 nm). The decoupling effect of sample $x=0.0$, as well as the intergranular

Table 7
Magnetic properties for the $SrFe_{12-x}Al_xO_{19}$ hexaferrites. Properties $\mu_0 M_{max}$, $\mu_0 M_r$, M_r/M_{max}, H_c, and T_c are experimental values, whereas K_1, $\mu_0 M_s$ and A are calculated parameters.

x	$\mu_0 M_{max}$ (T)	$\mu_0 M_r$ (T)	M_r/M_s	H_c (kA/m)	T_c (K)	K_1 (10^5 J/m^3)	$\mu_0 M_s$ (T)	A (10^{-12} J/m)
0.0	0.39	0.23	0.53	503	734	2.7	0.43	4.3
1.5	0.22	0.14	0.58	844	658	1.97	0.24	3.8

exchange interaction of sample $x=1.5$ are supported by the ratio M_r/M_s (with M_s estimated from the law of approach to saturation, as described below) for each sample, which are of 0.53 and 0.58, respectively (see Table 2). According to the Stoner–Wohlfarth model [18] for single domain, uniaxial, randomly oriented particles, the ratio $M_r/M_s=0.5$ indicates no interaction between particles and thus, the $M_r/M_s > 0.5$ values obtained for the $Fe_{12-x}Al_xO_{19}$ hexaferrites reflects that there exists some intergranular exchange interaction among constituents grains, mainly for the $x=1.5$ sample. A resume of magnetic properties is displayed in Table 7.

On the other hand, coercivity H_c displays a significant enhancement for increasing Al content, from 503 kA/m ($x=0.0$) to 844 kA/m ($x=1.5$). These remarkable values of H_c compare very well with the coercivity of rare-earth alloys of the type $Nd_8Fe_{86}B_6$, whose typical values lie around ~450 kA/m [7,8], as well as with the high-temperature $SmCo_7$ alloys, whose characteristic H_c values lie around 900 kA/m [15,16]. Complementary, we determine the magnetocrystalline anisotropy constant K_1 and the saturation magnetization $\mu_0 M_s$ for each composition from the law of approach to saturation for a distribution of uniaxial crystals [17]:

$$M(H) = M_s\left(1 - \frac{4}{15}\frac{K_1^2}{M_s^2}\frac{1}{H^2}\right) \quad (1)$$

K_1 for the $SrFe_{12-x}Al_xO_{19}$ hexaferrites varies from 2.7×10^5 J/m^3 ($x=0$) to 1.97×10^5 J/m^3 ($x=1.5$), whereas $\mu_0 M_s$ changes from 0.43 T ($x=0$) to 0.24 T ($x=1.5$). The decrease of K_1 can be ascribed to reduction of the unit cell (see Table 1), for which a diminished c parameter implies a less defined magnetization easy direction along the axial orientation. In addition, the modification of the 2b bipyramid site occupied by Fe^{3+} and Al^{3+} ions (described in the Rietveld fitting results) also hinders the easiness for the magnetization orientation along the c axis of the hexaferrites unit cell, and hence, causing the calculated decrease of the magnetocrystalline anisotropy constant K_1. The significant reduction of $\mu_0 M_s$ is attributed to the incorporation of the non-magnetic Al^{3+} cation into the 12k and 2b sites, which contributes significantly to the total magnetic moment per formula unit, since the magnetic moments of the Fe^{3+} cations at these sites couple parallel to the c direction within the unit cell, as described previously. From these data, the anisotropy field $H_A=2K_1/\mu_0 M_s$ for uniaxial, single domain particles [17], gives $H_A=1360$ kA/m (for $x=0$) and $H_A=1600$ kA/m (for $x=1.5$). This enhancement of H_A for the $SrFe_{10.5}Al_{1.5}O_{19}$ hexaferrite gives rise to its noticeable H_c value (844 kA/m).

In addition, MTGA curves of Fig. 7 show the characteristic Hopkinson peak at the Curie temperature (T_c). T_c exhibits a marked decrease for the $SrFe_{10.5}Al_{1.5}O_{19}$ hexaferrite (see Table 7). From T_c values, the exchange constant A for each composition can be estimated within the frame of the molecular field approximation as follows [18]:

$$A = \frac{3k_B T_c}{az} \quad (2)$$

where k_B is the Boltzmann constant, a is the unit cell parameter and z is the coordination number. From this expression, A decreases from 4.3×10^{-12} J/m ($x=0$) to 3.8×10^{-12} J/m ($x=1.5$). A summary of magnetic properties is given in Table 7.

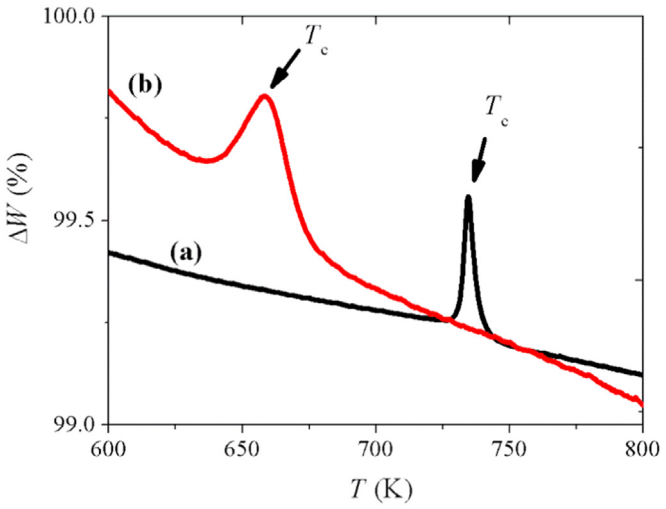

Fig. 7. Magnetic thermogravimetric curves for $SrFe_{12-x}Al_xO_{19}$ hexaferrites: (a) $x=0.0$ (b) $x=1.5$.

4. Discussion

The decreasing values of $\mu_0 M_s$ and T_c for the $SrFe_{12-x}Al_xO_{19}$ hexaferrites ($x=0.0,1.5$) are consistent with the incorporation of Al^{3+} cations into the crystal structure of the $SrFe_{12}O_{19}$ hexaferrite, since both properties are highly sensitive to the chemical composition. The reduction of $\mu_0 M_s$ is a consequence of the reduced magnetic moment per formula unit caused by the substitution of Fe by diamagnetic Al cations.

On the other hand, microstructural features, like grain size and phase distribution, play a significant role in the development of high H_c. In this context, a threshold parameter influencing the coercivity mechanism in hard magnetic materials is the critical diameter D_c for single domain particles. D_c can be calculated as follows [17]

$$D_c = \frac{72}{\mu_0 M_s^2}\sqrt{AK_1} \quad (3)$$

Based on the magnetic parameters of Table 7, we obtain for the $SrFe_{12-x}Al_xO_{19}$ hexaferrites $D_c=526$ nm for $x=0$ and $D_c=1358$ nm for $x=1.5$. By comparing these D_c data with the grain sizes determined from TEM observations, it is clear that our $SrFe_{12-x}Al_xO_{19}$ hexaferrites consist of single-domain particles. For materials comprising a random distribution of single-domain particles, enhanced H_c (relative to coarser, multi-domain grains) are possible because smaller crystals favor the magnetization reversal processes of the type coherent/incoherent rotation, depending on the grain size. The critical radius R_{coh} for coherent rotation is given by [19]:

$$R_{coh} = (24A/m_0 M_s^2)^{1/2} \quad (4)$$

For our $SrFe_{12}O_{19}$ phase, $R_{coh}=28.9$ nm. Therefore, it is clear that, for our hexaferrites with grain sizes around 60 nm $> R_{coh}$, the nucleation mode proceeds by incoherent rotation.

5. Conclusions

Pechini method is an efficient synthetic route to obtain nano-sized, single phase M-type $Sr(Fe,Al)_{12}O_{19}$ hexaferrites with enhanced coercivity values over 800 kA/m. Both, intrinsic and extrinsic magnetic properties were strongly influenced by the incorporation of the Al^{3+} cations into the crystal structure. Remarkable coercivity arises from the grain size refinement (below 60 nm), allowing an incoherent rotation mechanism for the magnetization reversal process, which favors the observed high coercivity values.

Acknowledgment

I.Betancourt acknowledges financial support from research project UNAM-PAPIIT IN104313. V. Barrera is grateful for the scholarship received from UNAM-PAPIIT IN104313. Special thanks are given for Adriana Tejeda, Carlos Flores and Damaris Cabrero (IIM-UNAM) for their valuable technical assistance.

References

[1] J.M.D. Coey, Permanent magnets: plugging the gap, Scr. Mater. 67 (2012) 524–529.
[2] O. Gutfleisch, M.A. Willard, E. Bruck, C.H. Chen, S.G. Sankar, J.P. Liu, Magnetic materials and devices for the 21st century: Stronger, lighter, and more energy efficient, Adv. Mater. 23 (2011) 821–842.
[3] R.K. Mudsainiyan, A.K. Jassal, M. Gupta, S.K. Chawla, Study on structural and magnetic properties of nanosized M-type Ba-hexaferrites synthesized by urea assisted citrate precursor route, J. Alloy. Compd. 645 (2015) 421–428.
[4] P. Kuruva, P.R. Matli, B. Mohammad, S. Reddigari, S. Katlakunta, Effect of Ni–Zr codoping on dielectric and magnetic properties of SrFe12O19 via sol-gel route, J. Magn. Magn. Mater. 382 (2015) 172–178.
[5] Y.M. Kang, Y.H. Kwon, M.H. Kim, D.Y. Lee, Enhacement of magnetic properties in Mn–Zn substituted M-type Sr-hexaferrites, J. Magn. Magn. Mater. 382 (2015) 10–14.
[6] K.H.J. Buschow, in: K.H.J. Buschow (Ed.), Concise encyclopedia of magnetic and superconducting materials, 2nd ed.,Elsevier, Amsterdam, 2005, pp. 14–16.
[7] I. Betancourt, H.A. Davies, Exchange coupled nanocomposite hard magnetic alloys, Mater. Sci. Technol. 26 (2010) 5.
[8] G.C. Hadjipanayis, Nanophase hard magnets, J. Magn. Magn. Mater. 200 (1999) 373–391.
[9] T. Kikuchi, T. Nakamura, T. Yamasaki, M. Nakanishi, T. Fujii, J. Takada, Y. Ikeda, Magnetic properties of La–Co substituted M-type strontium hexaferrites prepared by polymerizable complex method, J. Magn. Magn. Mater. 322 (2010) 2381–2385.
[10] P.E. Kazin, L.A. Trusov, D.D. Zaitsev, Yu.D. Tretyakov, M. Jansen, Formation of submicron-sized $SrFe_{12-x}Al_xO19$ with very high coercivity, J. Magn. Magn. Mater. 320 (2008) 1068–1072.
[11] T.T.V. Nga, N.P. Duong, T.D. Hien, Composition and magnetic studies of ultrafine Al-substituted Sr hexaferrite particles prepared by citrate sol-gel method, J. Magn. Magn. Mater. 324 (2012) 1141–1146.
[12] M.N. Ashiq, R.B. Qureshi, M.A. Malana, M.F. Ehsan, Synthesis, structural, magnetic and dielectric properties of zirconium copper doped M-type calcium strontium hexaferrites, J. Alloy. Compd. 617 (2014) 437–443.
[13] Y.J. Kwon, J. Ceram. Process Res. 3 (2002) 146.
[14] R.D. Shannon, Revised effective ionic radii and systematic studies of interatomic distances in halides and chalcogenides, Acta Cryst. A32 (1976) 751.
[15] Z. Zhang, X. Song, W. Xu, Phase evolution and its effects on the magnetic performance of nanocrystalline $SmCo_7$ alloy, Acta Mater. 59 (2011) 1808–1817.
[16] Z.X. Zhang, X.Y. Song, W.W. Xu, M. Seyring, M. Rettenmayr, Crystal structure and magnetic performance of single-phase nanocrystalline $SmCo_7$ alloys, Scr. Mater. 62 (2010) 594–597.
[17] H. Kronmuller, M. Fahnle, Micromagnetism and the microstructure of ferromagnetic solids, Cambridge University Press, Cambridge (2003), p. 176 105.
[18] B.D. Cullity, C.D. Graham, Introduction to magnetic materials, IEEE Press-Wiley, Hoboken, New Jersey, 2009.
[19] R. Skomski, J.M.D. Coey, Permanent magnetism, Institute of Physics Pub., Bristol, U.K., 1999.